DOI: 10.21062/mft.2026.012 http://www.journalmt.com

Study on Thermo-Structural Coupling Mechanism and Multi-Field Evolution Law during the Firing Process of Ceramic Slabs

Xianewei Wang (0000-0001-9804-0403)[1], Wenlong Xu (0009-0003-1815-6118)[1], Hailong Yu (0009-0008-3959-2214)[2], Chenyang Li (0009-0008-7418-6115)[1], Haikuo Zhao (0009-0000-8454-2656)[1], Yihang Feng (0009-0007-3229-2262)[1], Caiqi Fang (0009-0006-1381-4080)[1], Heng Zhang (0009-0008-9801-9821)[1], Aihua Xu (0000-0002-1604-8899)[3], Wentao Xie (0000-0002-3620-0245)[1], Xiulian Li (0000-0001-9441-261X)[1]
[1]Jiangsu University of Technology, Changzhou 213001, China. E-mail: wangxw@jsut.edu.cn, 2428741442@qq.com, 610498798@qq.com, 790887443@qq.com, okitasouji1234@outlook.com, 17798936757@163.com, Zhang204233@outlook.com,1262734188@qq.com, 936303415@qq.com, haikuo1412@163.com,
[2]Marco Polo Holdings Co., Ltd., Dongguan 523000, China. E-mail: 610498798@qq.com
[3] Changzhou Vocational Institute of Mechatronic Technology, Changzhou 213164, China. E-mail: xuah@ipp.ac.cn

To address cracking and deformation in large-size ceramic slabs during firing induced by thermo-structural coupling, this study established an indirect thermo-structural coupling finite element model in Ansys to analyze an 820 mm×100 mm×6.32 mm slab. The evolution of temperature field, stress field, and deformation was investigated across four firing stages. Results indicate that the rapid cooling stage, with a high convective heat transfer coefficient, forms the cycle's maximum thermal gradient, showing the most asymmetric temperature field of mid-plane high, surfaces low and a ~17°C surface-mid-plane temperature difference. The stress field follows a low-high-declining-stable trend, peaking in rapid cooling of 23 MPa maximum equivalent stress in the thickness section and 11 MPa maximum principal stress at the glaze-body interface. Thermal gradient, glaze-body CTE mismatch, and boundary constraints respectively drive stress generation, interface concentration, and asymmetric distribution. Deformation obeys length > width > thickness in rapid cooling, lengthwise deformation is 8.2 times the width. Thickness-direction drum-shaped deformation stems from glaze-body CTE mismatch. This study reveals the firing thermo-structural coupling mechanism, providing theoretical support for optimizing firing processes and glaze-body formulations, with significant engineering value for reducing cracking and improving dimensional stability.

Keywords: Ceramic slab, Thermo-structural coupling, Firing deformation, Maximum principal stress

1 Introduction

As a new type of large-size, high-strength architectural decoration material, ceramic slabs have witnessed rapidly growing application demands in high-end home decoration, commercial space finishing, and other fields in recent years, due to their excellent properties such as wear resistance, stain resistance, and high-temperature resistance [1-3]. The firing process, as the core link in slab production, directly determines the denseness of the product's microstructure, the stability of mechanical properties, and the consistency of appearance quality. However, due to the typical geometric characteristics of slabs-"large aspect ratio and small thickness"-coupled with the differences in thermal properties among the three-layer composite structure, ceramic slabs are susceptible to the combined effects of temperature gradients, thermal expansion mismatch of materials, and boundary constraints during the four firing stages. This leads to thermal stress concentration and uneven deformation, thereby causing quality defects such as glaze cracking and flatness deviation [4-8]. The temperature field is the root cause of thermal stress and thermal deformation, and its distribution uniformity and variation rate directly affect the intensity of thermo-structural coupling effects. Existing studies have explored the ceramic firing process: Li et al. [9-12] analyzed the influence of temperature gradients on cracking during the rapid cooling stage of traditional small-size ceramic tiles through numerical simulation, but they did not consider the regulatory effect of thermal property differences in the multi-layer structure of large-size slabs on the temperature field; Godet et al. [13-14] focused on the stress state at the glaze-body interface of slabs, yet failed to systematically establish a quantitative correlation between temperature field evolution and stress/deformation fields, making it difficult to comprehensively reveal the failure risk points in each firing stage. In addition, during the firing of large-size slabs, significant thermal deformation tends to occur in the length direction due to the geometric size effect. However, existing studies lack quantitative analysis of deformation laws in different directions, which cannot provide precise process parameter guidance for dimensional stability control.

To address the above research gaps, this study takes an 820 mm×100 mm×6.32 mm three-layer composite ceramic slab as the research object. An indirect thermo-structural coupling finite element model is established based on the Ansys platform. By introducing temperature-dependent material thermal properties and mechanical parameters, the temperature field distribution characteristics during the four firing stages are accurately simulated. The temperature field results are then input as loads into structural analysis to systematically investigate the distribution laws and evolution mechanisms of equivalent stress and maximum principal stress in each stage. Finally, the deformation differences in the length, width, and thickness directions of the slab are quantitatively analyzed, and the influence mechanisms of thermal gradients, material properties, and geometric dimensions on thermo-structural coupling effects are revealed, providing theoretical support for optimizing the slab firing process and improving glaze-body formulations.

2 Analysis of Temperature Field During Ceramic Slab Firing

2.1 Material Properties in Slab Firing Stages

Accurate analysis of the temperature field is crucial for controlling product quality and optimizing processes during ceramic slab firing. Considering that the influence of thermal radiation on the temperature field is far less significant than that of thermal conduction and convection [15], this study focuses on analyzing the effects of thermal conduction and convection. According to Fourier's law of heat conduction, the relationship between heat flux density q and temperature gradient ∇T is expressed as equation (1). Newton's law of cooling describes the heat exchange process between the object surface and the surrounding fluid, as shown in equation (2). By combining these two laws, the energy conservation equation for the thermal forming process of ceramic slabs can be established in equation 3. Through discretization of the energy conservation equation using the variational method, the finite element control equation for the temperature field during firing is derived, as presented in equation (4).

$$\vec{q} = -k\nabla T \; [\mathrm{W \cdot m^{-2}}] \,, \tag{1}$$

$$q = h(T - T_\infty) \; [\mathrm{W \cdot m^{-2}}] \,, \tag{2}$$

$$\rho c_p \frac{\partial T}{\partial t} = \nabla \cdot (k\nabla T) + h(T_\infty - T) \,, \tag{3}$$

$$[C]\{\dot{T}\} + [K]\{T\} = \{Q\} + \{H\} \,, \tag{4}$$

Where:

k…The thermal conductivity of the material [$\mathrm{W \cdot m^{-1} \cdot K^{-1}}$],

h…The convective heat transfer coefficient [$\mathrm{W \cdot m^{-2} \cdot K^{-1}}$],

T and T_∞…The temperature of the object and surrounding fluid respectively [K],

$[C]$ and $[K]$…The heat capacity matrix and thermal conductivity matrix respectively,

$\{\dot{T}\}$ …The first-order time derivative vector of temperature [$\mathrm{K \cdot s^{-1}}$],

$\{T\}$…The temperature vector [K],

$\{Q\}$…The internal heat source vector [$\mathrm{W \cdot m^{-3}}$],

$\{H\}$…The convective boundary heat flux vector [$\mathrm{W \cdot m^{-2}}$].

Table 1 lists the thermal conductivity and specific heat capacity of the slab body and glaze at different temperatures. With increasing temperature, the thermal conductivity of the body increases from 1.49 W/m·K at 22°C to 1.94 W/m·K at 1000°C, and the specific heat capacity increases from 721 J/kg·K to 1310 J/kg·K. The thermal conductivity and specific heat capacity of the glaze show the same variation trend as the body, but their values are generally higher than those of the body, reflecting the stronger heat conduction capability of the glaze. Table 2 presents the temperature ranges, convective heat transfer coefficients, and cooling gas temperatures for the four firing stages of the slab. The holding stage has the lowest convective heat transfer coefficient to maintain a constant temperature and uniform heat environment; the rapid cooling stage sees a sharp increase in the convective heat transfer coefficient to 27.17 W/m·°C, achieving rapid cooling through forced air cooling; the slow cooling stage reduces the convective heat transfer coefficient to 11.39 W/m·°C, creating conditions for internal stress release. And the final cooling stage uses a convective heat transfer coefficient of 24.03 W/m·°C to ensure the product cools steadily to room temperature. The cooling gas temperature in each stage is controlled at 30°C to eliminate interference from gas temperature fluctuations on the temperature field.

Tab. 1 *Thermal Properties of Ceramic Slabs*

Temp. (℃)	Body		Glaze	
	Thermal Conductivity (W/m·K)	Specific Heat Capacity (J/kg·K)	Thermal Conductivity (W/m·K)	Specific Heat Capacity (J/kg·K)
22	1.492	721	1.721	853
200	1.535	936	1.795	1115
400	1.542	1057	1.732	1212
600	1.648	1176	1.831	1344
800	1.727	1159	2.077	1458
1000	1.938	1310	2.496	1746

Tab. 2 *Key Parameters for Each Cooling Stage of Ceramic Tiles*

Cooling Stage	Temp. Variation Range	Convective Heat Transfer Coefficient (W/m·℃)	Cooling Gas Temp.(℃)
Holding Stage	1200~1100℃	8.418	30
Rapid Cooling Stage	1100~700℃	27.171	30
Slow Cooling Stage	700~500℃	11.394	30
Final Cooling Stage	500~RT	24.034	30

2.2 Temperature Field Simulation of Ceramic Slab Firing

A temperature field simulation of ceramic slabs was conducted via the Ansys Workbench platform, following these key steps. First, a 3D model was constructed based on the actual dimensions of the slab, with clear definition of its layered structure: body (5.82 mm), top glaze (0.2 mm), and bottom glaze (0.3 mm) (Figure 1A). For calculation accuracy, structured meshing was adopted. The overall element size was set to 2 mm, and mesh refinement was applied in the thickness direction, reducing the element size to 0.1 mm (Figure 1B). All mesh quality values exceeded 0.85, meeting the requirements for computational precision. Subsequently, boundary conditions were defined to match actual firing scenarios: the upper and lower surfaces of the slab were set as convective heat transfer boundaries (parameters listed in Table 2), while the side surfaces were designated as adiabatic boundaries. The transient thermal analysis module was selected, with a time step of 10 s and total simulation time aligned with the actual firing cycle of each stage. Prior to submitting the calculation, mesh convergence verification was performed to ensure that the influence of mesh size on the results was less than 5%. Through the above simulation, temperature field distributions on the thickness cross-section of the slab during the four firing stages were obtained in Figure 2. Specifically, Figure 2A shows the temperature field at the end of the holding stage, Figure 2B at the end of the rapid cooling stage, Figure 2C at the end of the slow cooling stage, and Figure 2D at the end of the final cooling stage.

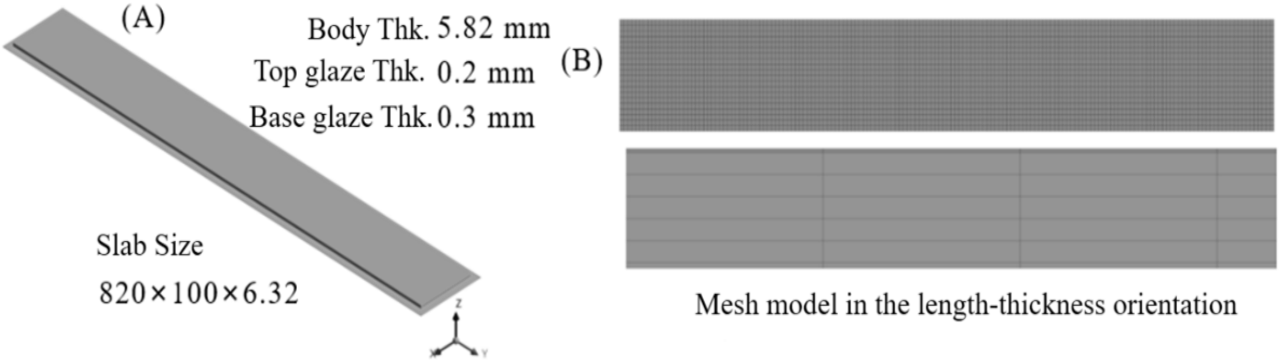

Fig. 1 *Structural Parameters and Finite Element Model of the Ceramic Slab*

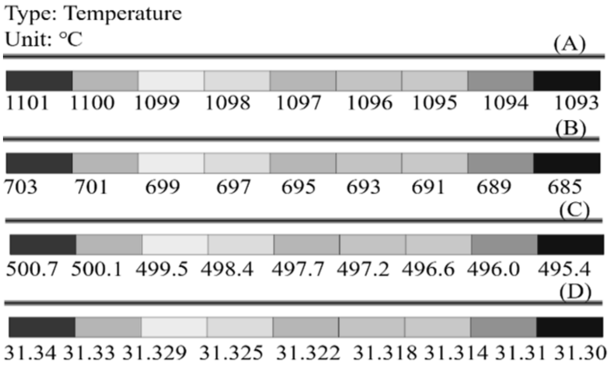

Fig. 2 *Temperature Field Distributions on the Thickness Cross-Section of Ceramic Slab During Four Firing Stages; (A) Temperature field distribution at the end of the 1st firing stage; (B) Temperature field distribution at the end of the 2nd firing stage; (C) Temperature field distribution at the end of the 3rd firing stage; (D) Temperature field distribution at the end of the 4th firing stage*

2.3 Results and Discussion

As indicated in Figure 2 (A)-(D), the temperature ranges across the four stages exhibit a stepwise decreasing trend. At the end of the holding stage, the temperature range of the slab's thickness cross-section is 1093.9~1101.2℃, with a temperature difference of only 7.3℃. This reflects the process objective of constant temperature and uniform heat during this stage, providing a stable thermal environment for the densification of the body during sintering and the melting and leveling of the glaze surface. During the rapid cooling stage, the temperature drops sharply to 685.8~702.62℃, with a single-stage cooling amplitude of 400℃ and the temperature difference expanding to 16.82℃. This is directly related to the highest convective heat transfer coefficient in this stage forced air cooling accelerates heat dissipation from the surface, creating a significant thermal gradient. In the slow cooling stage, the temperature further decreases to 495.42~500.72℃, and the temperature difference narrows to 5.3℃. The lower convective heat transfer coefficient slows down the cooling rate, creating conditions for the release of internal stress caused by the difference in thermal expansion coefficients between the body and glaze. At the end of the final cooling stage, the temperature approaches 30℃, with a temperature difference of only 0.69℃. The temperature field becomes nearly uniform, and the structural response tends to stabilize.

The temperature field in each stage exhibits a consistent distribution characteristic, high temperature is at the mid-plane and low temperature is at the upper and lower surfaces. It is because the upper and lower surfaces of the slab simultaneously undergo forced convective heat transfer with the cooling gas, while heat at the mid-plane of the thickness must be transferred to the surface through thermal conduction of the body, resulting in a thermal resistance lag effect. Among all stages, the asymmetry is most pronounced in the rapid cooling stage. the upper surface temperature is 685.8℃, the lower surface is 686.14℃, and the mid-plane reaches a maximum temperature of 702.62℃. The temperature differences between the upper surface and mid-plane, and between the lower surface and mid-plane, are 16.82℃ and 16.48℃, respectively far larger than those in other stages.

Combined with the thermal property data in Table 1, although the thermal conductivities of both the body and glaze decrease with temperature reduction in the range of 1100~700℃, the high convective heat transfer coefficient in the rapid cooling stage dominates the heat dissipation rate. This causes the thermal conduction rate between the surface and the interior to be unable to match the surface convective heat dissipation rate, ultimately forming the maximum thermal gradient.

3 Thermo-Structural Coupling Analysis of Ceramic Slab Firing

3.1 Fundamental Theory

The thermo-structural coupling analysis of ceramic slab firing is based on Fourier's law, Newton's law of cooling, and Hooke's law. Within the linear elastic range of the material, the stress-strain relationship induced by temperature field variations and thermal expansion coefficient differences satisfies Equations (5) and (6). For calculating the stress-strain field of ceramic slabs, two approaches are available, namely the direct coupling and indirect coupling. Direct coupling method solves thermal and structural equations simultaneously within a single finite element model. It integrates temperature- and displacement-related degrees of freedom into a complete coupled equation system shown in Equation 7. This method offers high computational efficiency and captures the real-time interaction between thermal and structural fields. However, it demands substantial computational resources and involves greater complexity in model construction and solution. Indirect coupling method follows a two-step process. First, it solves the temperature field distribution through thermal analysis. Second, it applies the temperature results as a load to the structural analysis model, then solves for stress and deformation using structural mechanics equations shown in Equation 8. This method features simplicity in operation and low requirements for computational resources, making it well-suited for the engineering problem addressed in this study. Thus, the indirect coupling method is adopted for the analysis.

$$\sigma_{ij} = C_{ijkl}\left(\epsilon_{kl} - \alpha_{kl}\Delta T\delta_{ij}\right) \text{ [Pa]}, \tag{5}$$

$$\epsilon_{ij} = \frac{1}{2}\left(\frac{\partial u_i}{\partial x_j} + \frac{\partial u_j}{\partial x_i}\right) + \alpha_{ij} + (T - T_0)\delta_{ij}\,, \tag{6}$$

$$\begin{bmatrix} K_{TT} & K_{TS} \\ K_{ST} & K_{SS} \end{bmatrix}\begin{Bmatrix} T \\ U \end{Bmatrix} = \begin{Bmatrix} Q_T \\ F_S \end{Bmatrix}, \tag{7}$$

$$[K_S]\{\mathrm{U}\} = \{F_S^{th}\} + \{F_S^{ext}\}\,, \tag{8}$$

Where:

C_{ijkl} and σ_{ij} …The elastic constant tensor and stress tensor respectively [Pa],

ϵ_{kl} and δ_{ij} …The strain tensor and Kronecker delta respectively,

α…The thermal expansion coefficient [K^{-1}],

T and T_0…The current and reference temperatures respectively [K],

u_i, u_j and x, x_j …The displacement component and spatial coordinate respectively [m],

K_{TT} and K_{ST}…The thermal conductivity and thermo-structural coupling matrices respectively [$W\cdot m^{-1}\cdot K^{-1}$],

K_{SS} and $[K_S]$…The structural stiffness matrices [$N\cdot m^{-1}$],

U and $\{U\}$…The displacement vectors [m],

Q_T, $\{F_S^{th}\}$, $\{F_S^{ext}\}$…The thermal load vector, temperature induced thermal load vector and external mechanical load vector respectively [W],

F_S…The mechanical load vector [N].

3.2 Thermo-Structural Coupling Simulation

The indirect thermo-structural coupling analysis using Ansys consists of two key phases, namely the thermal analysis and structural analysis [16-18]. In the thermal analysis phase, following the geometric modeling and meshing scheme detailed in Section 2.2, temperature-dependent thermal properties of the material are input. Convective heat transfer boundary conditions for each firing stage are defined in accordance with Table 2. The transient thermal analysis module is selected for computation, yielding the temperature field distribution results across the four firing stages. In the structural analysis phase, First, the element type of the thermal analysis model is converted from thermal elements to structural elements. This ensures consistent mesh topology, eliminating calculation errors caused by mesh discrepancies. Next, temperature-dependent mechanical parameters for each component of the slab are input shown Table 3. To simulate actual firing conditions. The contact area between the slab's lower surface and the rigid base plate is set as a fixed constraint. The upper surface and side surfaces are defined as free boundaries to avoid interference from unnecessary constraints on deformation calculations. Finally, the temperature field results from the thermal analysis are applied to the structural model as a body temperature load. The static structural analysis module is selected, and solution step sizes are configured to capture stress mutations induced by temperature changes. Upon submitting the calculation, the stress field and deformation field distributions for each stage are obtained.

***Tab. 3** Mechanical Properties of Ceramic Slabs at Different Temperatures*

	Body			Glaze		
Temp.(°C)	CTE (×10^{-6})	E (MPa)	μ	CTE (×10^{-6})	E (MPa)	μ
22	-	76700	0.24	-	76700	0.24
200	6.3	-	-	5.4	-	-
400	7.03	-	-	6.09	-	-
600	8.25	-	-	6.5	-	-
800	7.4	79570	0.23	7.3	79570	0.23
1000	-	73220	0.25	-	73220	0.25
1200	-	71820	0.26	-	71820	0.26

Where:

CTE…The Coefficient of Thermal Expansion,

E…The Elastic Modulus,

μ…The Poisson's ratio.

3.3 Distribution Law of Equivalent Stress

Structural analysis yielded the equivalent stress distributions of the ceramic slab across the four firing stages (Figs. 3-6). Specifically, Fig. 3 shows the equivalent stress during the holding stage, Fig. 4 is during the rapid cooling stage, Fig. 5 is during the slow cooling stage, and Fig. 6 is during the final cooling stage. In each figure, (A) represents the equivalent stress on the upper surface, (B) represents the equivalent stress on the lower surface, and (C) represents the equivalent stress on the thickness cross-section. As indicated in Figs. 3-6, the equivalent stress of the slab exhibits a four-stage of "low-high-declining-stable" trend throughout the firing process.

In the holding stage, the equivalent stress remains at an overall low level, the maximum equivalent stress is 7.32 MPa on the upper surface, 6.90 MPa on the lower surface, and 7.32 MPa on the thickness cross-section. The stress distribution is uniform with no obvious concentration zones. This phenomenon arises from two key factors. First, the minimal temperature difference in the holding stage results in small thermal strains induced by the mismatch in thermal expansion coefficients between the body and glaze. Second, the low elastic modulus and high plasticity of both the body and glaze at this stage allow partial thermal stress release through micro-plastic deformation, leading to an overall low stress level.

In the rapid cooling stage, the equivalent stress reaches its peak, with the maximum value on the thickness cross-section reaching 23.4 MPa-3.4 times higher than that in the holding stage. The upper surface exhibits a maximum stress of 22.63 MPa, exceeding the lower surface's 19.67 MPa. This discrepancy stems from two mechanisms. One is the thermal gradient effect. The maximum thermal gradient of 16.8 ℃ during rapid cooling induces significant thermal contraction mismatch. The upper and lower surfaces cool faster and contract more, while the mid-plane cools slower with less contraction. This creates a constraint effect where the mid-plane restrains surface contraction, generating tensile stress on the surfaces. Larger thermal gradients intensify this constraint, amplifying tensile stress. The other is the mechanical constraint effect. The slab's lower surface contacts a rigid base plate, whose mechanical constraint partially offsets the lower surface's tensile stress. In contrast, the unconstrained upper surface allows full release of tensile stress, resulting in higher stress than the lower surface. Additionally, the glaze's CTE is lower than the body's in this stage, causing the body to contract more than the glaze. This creates tensile restraint of the glaze by the body, making the glaze prone to micro-cracking-consistent with industrial observations that glaze cracking rates peak during rapid cooling.

In the slow cooling stage, Equivalent stress decreases significantly compared to the rapid cooling stage, 19.91 MPa of the upper surface, 18.63 MPa of the lower surface, and 19.08 MPa of the thickness cross-section, representing a 12.0-18.4% reduction. The key drivers of stress reduction include. A lower convective heat transfer coefficient slows cooling, narrowing the thickness-direction temperature difference to 5.3 ℃ and weakening the constraint effect induced by thermal gradients. In the 700-500℃ range, the elastic modulus of the body and glaze gradually increases with decreasing temperature, but the material retains sufficient plasticity to further release residual stress accumulated during rapid cooling. This results in a more uniform stress distribution, with the stress difference between upper and lower surfaces narrowing to 1.28 MPa.

In the final cooling stage, as temperature approaches room temperature, equivalent stress drops to its lowest level, 6.0 MPa of the upper surface, 5.46 MPa of the lower surface, and 6.0 MPa of the thickness cross-section-comparable to the holding stage but with a more uniform distribution. This is because the nearly uniform temperature field minimizes thermal strain, leaving primarily residual thermal stress-the portion of thermal stress not fully released in previous stages. This residual stress, positively correlated with the peak stress in the rapid cooling stage, is concentrated at the glaze-body interface, posing a potential risk for interface failure during the slab's service life.

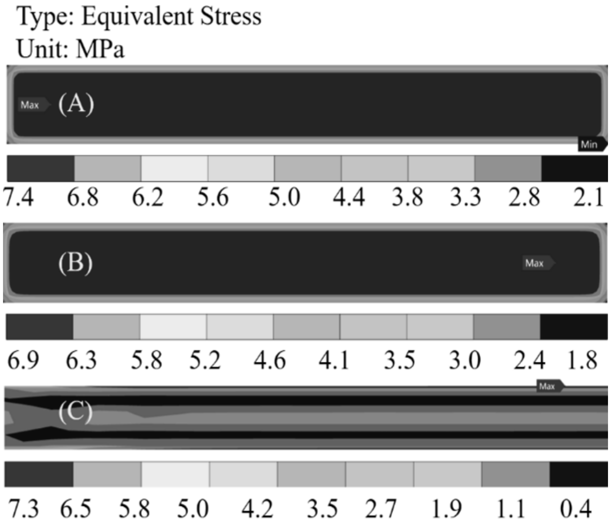

Fig. 3 *Equivalent Stress on the Upper Surface, Lower Surface, and Thickness Cross-Section of Ceramic Slab in the 1st Firing Stage; (A) Equivalent stress distribution on the upper surface; (B) Equivalent stress distribution on the lower surface; (C) Equivalent stress distribution on the thickness cross-section*

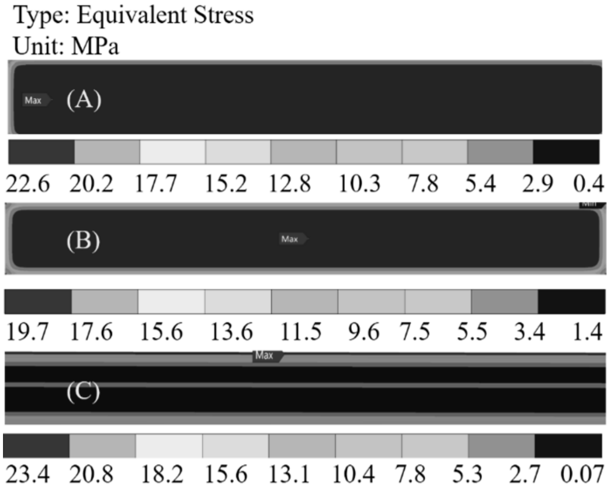

Fig. 4 *Equivalent Stress on the Upper Surface, Lower Surface, and Thickness Cross-Section of Ceramic Slab in the 2nd Firing Stage; (A) Equivalent stress distribution on the upper surface; (B) Equivalent stress distribution on the lower surface; (C) Equivalent stress distribution on the thickness cross-section*

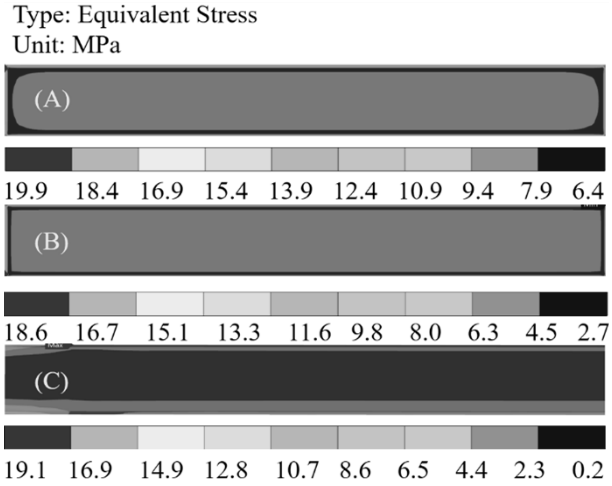

Fig. 5 *Equivalent Stress on the Upper Surface, Lower Surface, and Thickness Cross-Section of Ceramic Slab in the 3rd Firing Stage; (A) Equivalent stress distribution on the upper surface; (B) Equivalent stress distribution on the lower surface; (C) Equivalent stress distribution on the thickness cross-section*

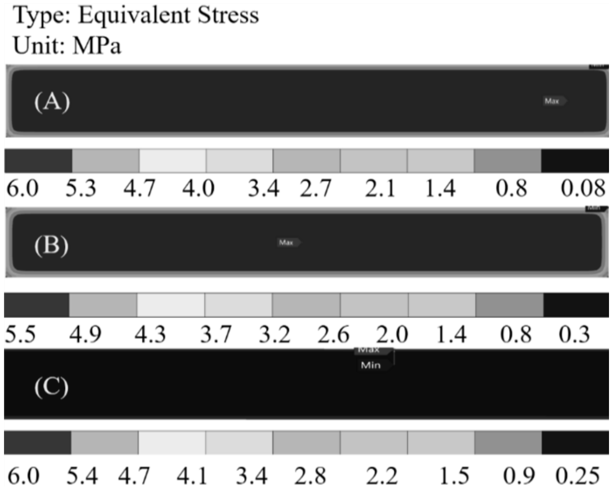

Fig. 6 *Equivalent Stress on the Upper Surface, Lower Surface, and Thickness Cross-Section of Ceramic Slab in the 4th Firing Stage; (A) Equivalent stress distribution on the upper surface; (B) Equivalent stress distribution on the lower surface; (C) Equivalent stress distribution on the thickness cross-section*

3.4 Evolution Law of Maximum Principal Stress

Figs. 7-10 illustrate the maximum principal stress variation along two typical thickness paths of the ceramic slab across the four firing stages. Path A is the thickness path at the slab's end, and Path B is the thickness path at the slab's center, both extending from the lower surface to the upper surface. Specifically, Fig. 7 corresponds to the holding stage, Fig. 8 to the rapid cooling stage, Fig. 9 to the slow cooling stage, and Fig. 10 to the final cooling stage. During the holding stage, along both Path A and Path B, the maximum principal stress exhibits an approximately symmetric high at both ends, low in the middle distribution. The maximum principal stress in the glaze layer is approximately 7 MPa, significantly higher than that in the body. The stress peak is located on the upper surface of the top glaze, while the maximum principal stress approaches zero at the slab's mid-plane. Additionally, the maximum principal stress at the slab's center (Path B) is slightly higher than that at the end (Path A), which is attributed to the more uniform temperature and stronger thermal strain coordination capability in the central region. During the rapid cooling stage, the stress distribution retains the high at both ends, low in the middle pattern, but the maximum principal stress peak shifts from the surface to the glaze-body interface, reaching approximately 11 MPa-far exceeding the peak stress in the 1st stage. The maximum principal stress approaches zero inside the glaze layer and near the body's mid-plane. Furthermore, along Path A, the maximum principal stress near the body's mid-plane is negative, consistent with the more pronounced thermal gradient and stronger constraint effect in the end region. During the slow cooling stage, the high at both ends, low in the middle distribution persists, with the maximum principal stress peak remaining at the glaze-body interface but decreasing significantly in magnitude: ~6.8 MPa at the slab's center (Path B) and ~4.2 MPa at the end (Path A). The maximum principal stress approaches zero inside the glaze layer and near the body's mid-plane. The stress difference between the two paths expands to 2.6 MPa, reflecting more sufficient stress release in the end region-due to more direct heat exchange with the external environment and more pronounced stress relaxation induced by deformation. During the final cooling stage, the stress distribution pattern transitions from high at both ends, low in the middle to unidirectional decrease from the bottom glaze surface to the top glaze surface. Along both Path A and Path B, stress peaks at the bottom glaze-body interface, then decreases approximately linearly along the thickness direction, reaching a minimum at the body-top glaze interface. The maximum principal stress inside the glaze layer approaches zero, and the stress difference between the two paths narrows to 0.05 MPa. The overall stress level is significantly lower than in the previous three stages, indicating that the slab has largely completed stress release and tends to stabilize.

The evolutionary mechanism of the maximum principal stress distribution pattern varies by stage. In the 1st Stage, dominated by the temperature gradient between the slab's surface and center. In the 2nd & 3rd Stages, Controlled by the thermal expansion coefficient mismatch between the body and glaze. In the 4th Stage, thermal stress is effectively released due to reduced temperature gradients, leading to a more uniform stress distribution.

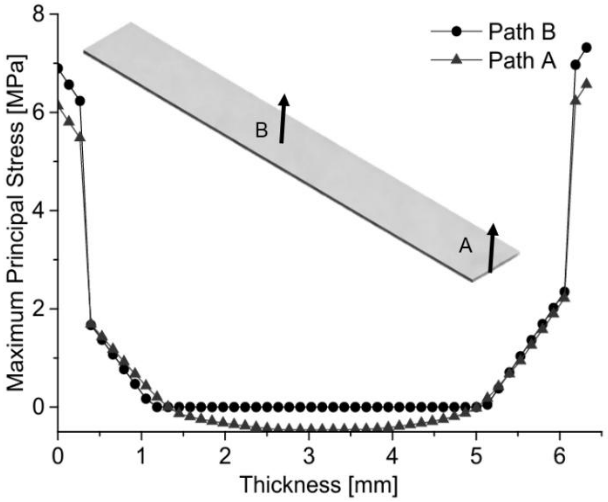

Fig. 7 *Maximum Principal Stress Along Different Thickness Paths of Ceramic Slab in the 1st Firing Stage*

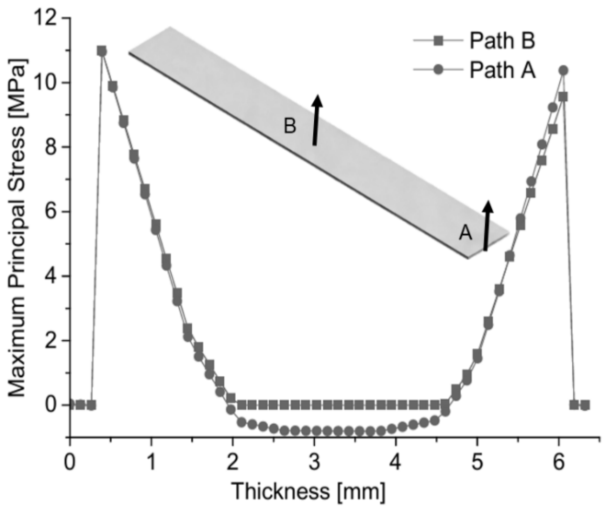

Fig. 8 *Maximum Principal Stress Along Different Thickness Paths of Ceramic Slab in the 2nd Firing Stage*

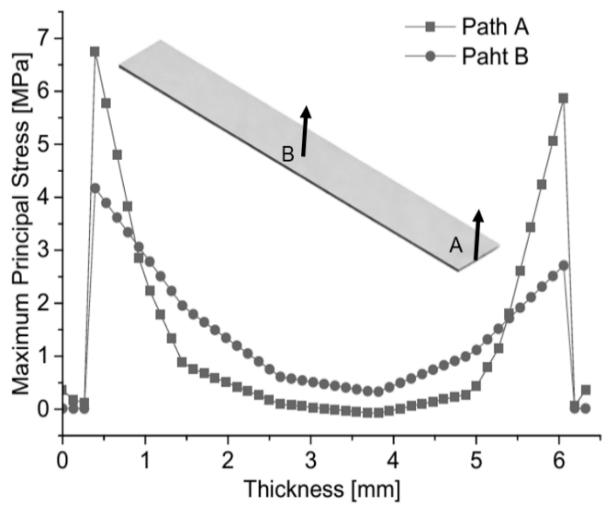

Fig. 9 *Maximum Principal Stress Along Different Thickness Paths of Ceramic Slab in the 3rd Firing Stage*

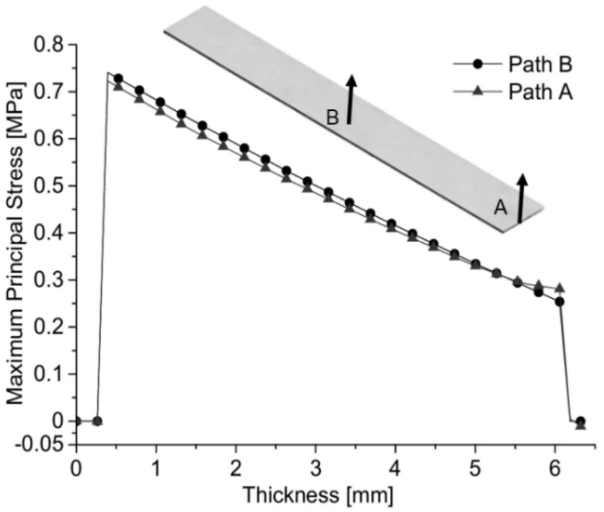

Fig. 10 *Maximum Principal Stress Along Different Thickness Paths of Ceramic Slab in the 4th Firing Stage*

3.5 Distribution Law of Deformation

Figs. 11-14 present the deformation quantities of ceramic slabs across the four firing stages. Specifically, Fig. 11 corresponds to the holding stage, Fig. 12 to the rapid cooling stage, Fig. 13 to the slow cooling stage, and Fig. 14 to the final cooling stage. In each figure, (A) is the deformation in the width direction. (B) is the deformation in the length direction. (C) is the deformation in the thickness direction. In all stages, deformation follows the consistent trend, length direction > width direction > thickness direction. This discrepancy arises from the slab's geometric size effect, the length is significantly larger than the width and thickness. According to the thermal deformation formula, under the same thermal expansion coefficient and temperature difference, a longer original dimension results in greater thermal deformation. Thus, the length direction is identified as the key direction for controlling the slab's dimensional stability.

The deformation quantity across the four stages follows the order, rapid cooling stage > slow cooling stage > final cooling stage > holding stage. In the holding stage shown in Figure 11, deformation is minimal. The maximum deformation reaches 0.31 mm in the length direction, and 0.04 mm in both the width and thickness directions. This is attributed to the uniform temperature field, which enables coordinated thermal strain without significant deformation variation. In the rapid cooling stage shown in Figure 12, deformation is maximum. The length direction deformation reaches 1.28 mm-3.1 times higher than that in the holding stage. The large thermal gradient induces severe thermal contraction mismatch, and the material retains sufficient plasticity at this stage to undergo substantial plastic deformation, leading to the peak deformation. In the slow cooling stage shown in Figure 13, deformation decreases significantly. The length direction deformation drops to 0.61 mm, a 52.4% reduction from the rapid cooling stage. The reduced cooling rate minimizes thermal contraction mismatch, and part of the plastic deformation is recovered through stress release, resulting in lower overall deformation. In the final cooling stage shown in Figure in 14, deformation is stabilized. The length direction deformation further decreases to 0.18 mm, a 71.0% reduction from the slow cooling stage. The uniform temperature field halts thermal deformation, and the remaining residual deformation is primarily composed of elastic deformation induced by residual stress.

Deformation in the thickness direction exhibits the feature, shrinkage of upper and lower glaze surfaces is larger than the shrinkage of the body center. Taking the rapid cooling stage as an example, the maximum deformation in the thickness direction is 0.40 mm, with the upper glaze surface showing slightly greater deformation than the lower glaze surface. This phenomenon is driven by two factors. One is that CTE mismatch between glaze and body. The glaze has a lower CTE than the body. During cooling, the body tends to shrink more than the glaze, but the glaze-covering the body surface-is stretched by the body's contraction. This causes the glaze surfaces to form slight outward bulges, resulting in drum-shaped deformation in the thickness direction. The other is that the boundary constraint is different. The upper glaze surface is free of mechanical constraints, allowing more unrestricted deformation, while the lower glaze surface is partially constrained by the rigid base plate. This explains why the upper glaze surface exhibits slightly larger deformation. This minor drum-shaped deformation in the thickness direction may cause surface flatness deviations in actual production. It can be controlled by adjusting the glaze layer thickness or optimizing the CTE matching between the body and glaze.

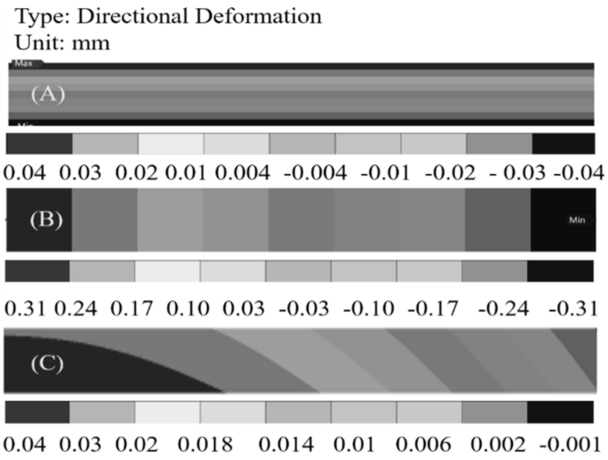

Fig. 11 *Deformation of Ceramic Slab in Various Directions During the 1st Firing Stage; (A) is the deformation of the slab in the width direction; (B) is the deformation of the slab in the length direction; (C) is the deformation of the slab in the thickness direction*

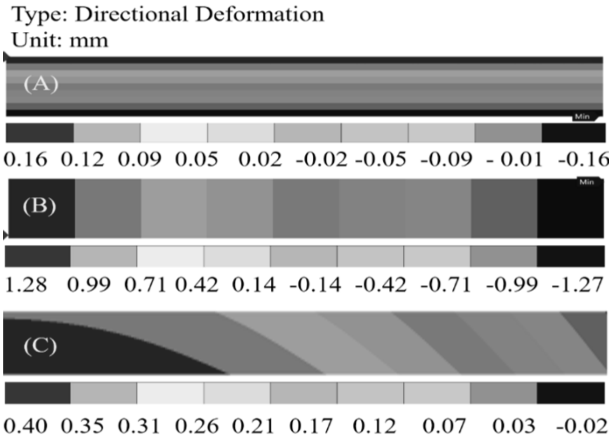

Fig. 12 *Deformation of Ceramic Slab in Various Directions During the 2nd Firing Stage; (A) is the deformation of the slab in the width direction; (B) is the deformation of the slab in the length direction; (C) is the deformation of the slab in the thickness direction*

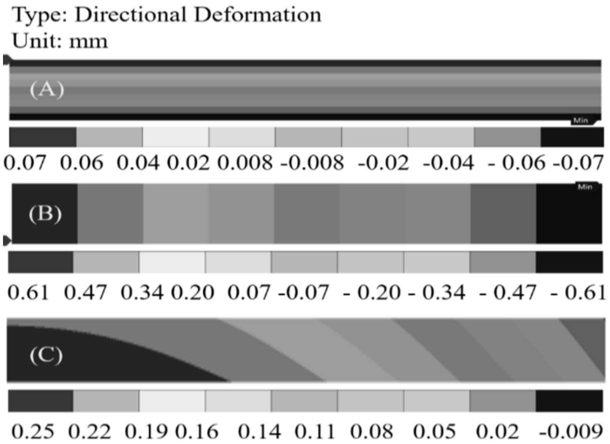

Fig. 13 *Deformation of Ceramic Slab in Various Directions During the 3rd Firing Stage; (A) is the deformation of the slab in the width direction; (B) is the deformation of the slab in the length direction; (C) is the deformation of the slab in the thickness direction*

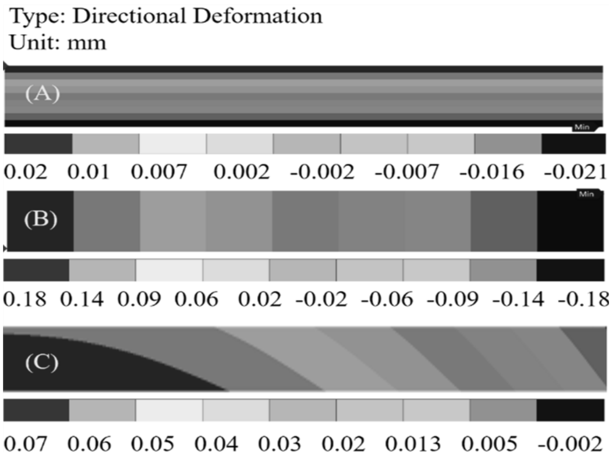

Fig. 14 *Deformation of Ceramic Slab in Various Directions During the 4th Firing Stage; (A) is the deformation of the slab in the width direction; (B) is the deformation of the slab in the length direction; (C) is the deformation of the slab in the thickness direction*

4 Conclusions

Based on the Ansys platform, this study established an indirect thermo-structural coupling finite element model to systematically analyze the temperature field, stress field, and deformation behavior of ceramic slabs during the four firing stages. The thermo-structural coupling mechanism was quantitatively revealed, providing theoretical support for the optimization of slab firing processes and quality control. The key conclusions are as follows:

- (1) The temperature range of the four firing stages decreases in a stepwise manner. In the holding stage, the temperature difference across the thickness cross-section is only 7.3℃, providing a stable thermal environment for body sintering and glaze leveling. In the rapid cooling stage, due to the high convective heat transfer coefficient, the temperature drops by 400℃ in this single stage, and the temperature difference expands to 16.82℃-the largest thermal gradient in the entire firing cycle. In the slow cooling and final cooling stages. The temperature differences gradually narrow to 5.3℃ and 0.69℃, respectively, with the temperature field becoming increasingly uniform. Across all stages, the temperature field exhibits a consistent distribution pattern of higher temperature at the mid-plane, lower temperature at the upper and lower surfaces. The asymmetry is most pronounced in the rapid cooling stage, where the temperature difference between the upper/lower surfaces and the mid-plane reaches approximately 17℃. This inhomogeneity is attributed to the thermal resistance lag effect.
- (2) The stress field undergoes a four-stage of low-high-declining-stable trend during firing. In the holding stage, the equivalent stress is the lowest and uniformly distributed. In the rapid cooling stage, stress reaches the peak value, with the maximum equivalent stress on the thickness cross-section reaching 23.4 MPa-3.4 times higher than that in the holding stage. The upper surface stress exceeds the lower surface stress, resulting from two combined effects, the thermal contraction constraint induced by the large thermal gradient, and the stress-offset effect of the mechanical constraint from the rigid base plate on the lower surface. In the slow cooling stage, stress decreases by 12.0-18.4% and becomes more uniform. In the cooling stage, Stress returns to a low level, with residual stress concentrated at the glaze-body interface. The maximum principal stress distribution evolves from an approximately symmetric high at both ends, low in the middle pattern in the early stages to a unidirectional decrease from bottom glaze to top glaze trend in the final cooling stage. During rapid cooling, the maximum principal stress at the glaze-body interface reaches 11 MPa-identified as the high-risk zone for slab cracking. To reduce the cracking risk of ceramic slabs, adjustments should be made to the convective heat transfer coefficient during the rapid cooling stage and the glaze composition to minimize the thermal expansion coefficient mismatch between the body and glaze, thereby alleviating stress concentration at the interface.
- (3) In all stages, deformation follows the consistent rule, length direction > width direction > thickness direction. The rapid cooling stage exhibits the largest deformation, with a maximum value of 1.274 mm in the length direction-8.2 times that of the width direction and 3.2 times that of the thickness direction. The geometric size effect dominates the directional differences in deformation. Deformation in the thickness direction is characterized by greater shrinkage of upper/lower glaze surfaces than the body center. During rapid cooling, the upper glaze surface shows slightly larger deformation than the lower glaze surface, driven by two factors. Namely，The tensile drum-shaped deformation caused by the glaze’s lower CTE compared to the body. And the unconstrained upper surface, which allows more free deformation than the mechanically constrained lower surface.

Acknowledgement

This project has been financially supported by the the Applied Research Program of Marco Polo (Grant No. KYH25210) and the Project of Background Field Magnets (Grant No. KYH20148).

References

[1] SIMONA DE NIEDERHÃUSERN, M. BONDI, AND F. BONDIOLI. (2013). Self‐Cleaning and Antibacteric Ceramic Tile Surface. In: *International Journal of Applied Ceramic Technology*, Vol. 10, No. 6, pp. 949-956.

[2] KUISMA, RISTO, et al. (2007). Microstructure and cleanability of uncoated and fluoropolymer, zirconia and titania coated ceramic glazed surfaces. In: *Journal of the European Ceramic Society*, Vol. 27, No. 1, pp.101-108.

[3] WANG, SHAOHUA, et al. (2020). Corrosion resistance and cleanability of glazed surface. In: *International Journal of Applied Ceramic Technology.*, Vol. 17, No. 5, pp. 2162-2170.

[4] CHEN T, GONG B, TANG C. (2023). Origin and Evolution of Cracks in the Glaze Surface of a Ceramic during the Cooling Process. In: *Materials.*, Vol. 16, No. 16, pp. 5508.

[5] JUNIOR, JAMILSON PINTER, et al. (2022). Novel approach to ensure the dimensional stability of large-format enameled porcelain stoneware tiles through water absorption control. In: *Open Ceramics*, Vol. 9, pp.100203.

[6] FAZILET GUNGOR. (2018). Investigation of pyroplastic deformation of whitewares: Effect of crystal phases in the "CaO" based glassy matrix. In: *Ceramics International*, Vol. 44, No. 11, pp.13360-13366.

[7] KAVANOVA, MARIA, et al. (2017). Characterization of the interaction between glazes and ceramic bodies. In: *Ceramics Silikaty,* Vol. 61, No. 3, pp. 267-275.

[8] CONSERVA, LISANDRA R. DOS SANTOS, et al. (2017). Pyroclastic deformation of porcelain stoneware tiles: Wet vs. dry processing. In: *Journal of the European Ceramic Society.*, Vol. 37, No. 1, pp. 333-342.

[9] DINGYU LI, YONG PANG, TAO LU, et al. (2022). Numerical Analysis of Thermal Shock Cracking Behaviors of Ceramics Based on the Force-Heat Equivalence Energy Density Principle. In: *Front. Mater*, Vol. 8, pp. 1-9.

[10] LI D, WANG R, WANG X, et al. (2020). Simulation of the thermal shock cracking behaviors of ceramics under water quenching for 3-dimension conditions. In: *European Journal of Mechanics*, Vol. 84, pp.104080.

[11] YONG PANG, DINGYU LI, XIN LI, et al. (2013). Phase-Field Simulation of Temperature-Dependent Thermal Shock Fracture of Al2O3/ZrO2 Multilayer Ceramics with Phase Transition Residual Stress. In: *Materials*, Vol. 16, No. 2, pp. 734.

[12] MARCELO DAL BÓ, et al. (2012). Mechanical Modelling of Rapid Cooling in Porcelain Tile-Type Systems. In: *Boletin de la Sociedad Espanola de Ceramicay Vidrio*, Vol. 52, No. 2, pp. 95-102.

[13] GODET MARIE, GAUTHIER ROISINE, et al. (2019). Multi-Scale Investigation of Body-Glaze Interface in Ancient Ceramics. In: *Heritage*, Vol. 2, No. 3, pp. 2480-2494.

[14] DOUGLAS FABRIS, JÚLIO C.M. SOUZA, FILIPE S. SILVA, et al. (2017). Thermal residual stresses in bilayered, trilayered and graded dental ceramics. In: *Ceramics International.*, Vol. 43, No. 4, pp. 3670-3678.

[15] OBA, R., T. S. POSSAMAI, AND V. P. NICOLAU. (2014). Thermal analysis of a tunnel kiln used to produce roof tiles. In: *Applied Thermal Engineering*, Vol. 63, No. 1, pp. 59-65.

[16] KOZOVÝ, P., M. ŠAJGALÍK, M. DRBÚL, et al. (2023). Identification of Residual Stresses after Machining a Gearwheel Made by Sintering Metal Powder. In: *Manufacturing Technology*, Vol. 23, No. 4, pp. 468-474.

[17] ANASIEWICZ, K., J. JÓZWIK, M. LELEŃ, P. PIEŚKO, et al. (2024). Identification of Internal Defects in Forged Shafts by Measurement of Residual Stresses Using X-Ray Method. In: *Manufacturing Technology*, Vol. 24, No. 5, pp. 711-720.

[18] SHEU, J. J., AND E. H. CHIEN. (2025). Process Prediction and Force Measurement of Hot Rolling Process for 6061 Aluminum Alloy Wire. In: *Manufacturing Technology*, Vol. 25, No. 3, pp. 383-395.